

# Analyst

Accepted Manuscript

This article can be cited before page numbers have been issued, to do this please use: C. He, H. Liu, M. Yin, J. Chen, W. Huang, H. Zhou, S. Wu and Y. Wang, *Analyst*, 2025, DOI: 10.1039/D4AN01512F.



This is an Accepted Manuscript, which has been through the Royal Society of Chemistry peer review process and has been accepted for publication.

Accepted Manuscripts are published online shortly after acceptance, before technical editing, formatting and proof reading. Using this free service, authors can make their results available to the community, in citable form, before we publish the edited article. We will replace this Accepted Manuscript with the edited and formatted Advance Article as soon as it is available.

You can find more information about Accepted Manuscripts in the [Information for Authors](#).

Please note that technical editing may introduce minor changes to the text and/or graphics, which may alter content. The journal's standard [Terms & Conditions](#) and the [Ethical guidelines](#) still apply. In no event shall the Royal Society of Chemistry be held responsible for any errors or omissions in this Accepted Manuscript or any consequences arising from the use of any information it contains.

## ARTICLE

**UOx@HMnO<sub>2</sub> Biozyme-Nanozyme Driven Electrochemical Platform for Specific Uric Acid Bioassays**Chenlong He<sup>1,a</sup>, Huawei Liu<sup>1,a</sup>, Ming Yin<sup>a</sup>, Jing Chen<sup>a</sup>, Wensi Huang<sup>b</sup>, Han Zhou<sup>a</sup>, Shengming Wu<sup>a</sup>, Yilong Wang<sup>\*,a</sup>Received 00th January 20xx,  
Accepted 00th January 20xx

DOI: 10.1039/x0xx00000x

Uric acid (UA) is a key end product of purine metabolism in the human body, and its abnormal level is associated with many diseases, so accurate monitoring is essential. Existing detection methods have many limitations, such as chromatography, which is cumbersome, time-consuming, and not cost-effective, and serum uric acid analysis, which requires specialized equipment and venous blood collection. In the field of uric acid sensors, electrochemical detection is commonly used but prone to interference, and nanomaterials are improved but complicated to modify. To better block the interference via an easily-made nanocomposites involved system, in this study, MnO<sub>2</sub> with peroxidase-mimicking activity was used as a protective shell to encapsulate natural uric acid oxidase (UOx), realizing good combination of nanozymes and biocatalysts. The UOx can selectively catalyze UA and generate H<sub>2</sub>O<sub>2</sub>, and the MnO<sub>2</sub> nanozymes can make up for the insufficiency of UOx, and the two main components synergistically make the activity of UOx@HMnO<sub>2</sub> ultra-high, which can offer simple and versatile methods to prepare highly efficient hybrid biocatalysts for the fields of biosensors and biocatalysis. This provides a simple and general method for the preparation of efficient hybridized biocatalysts in the fields of biosensors and biocatalysis. The detection limit of the fabricated uric acid sensor is as low as 0.74 μM, and the concentration of the actual sample is consistent with that of mass spectrometry, which provides a means of non-invasive detection of uric acid with high sensitivity, high specificity and good accuracy.

**Introduction**

The main text of the article should appear here with headings as appropriate. Uric acid (UA, C<sub>5</sub>H<sub>4</sub>N<sub>4</sub>O<sub>3</sub>) is a key end product of purine metabolism in the human body, and is excreted primarily in the urine to maintain homeostasis of uric acid levels in the body. In healthy individuals, serum uric acid concentrations are usually maintained between 120.0 and 520.0 μM, while urinary uric acid concentrations range from 1.4 to 4.4 mM.<sup>1,2</sup> Abnormal uric acid levels are closely associated with a variety of diseases, including but not limited to gout, kidney disease, Lesch-Nyhan syndrome, cardiovascular disease and metabolic syndrome.<sup>3</sup> Therefore, accurate monitoring of uric acid levels is essential for early diagnosis, effective treatment and long-term follow-up of related diseases.<sup>4</sup> However, existing uric acid testing methods, such as high-performance liquid chromatography (HPLC) and gas chromatography (GC), are not only cumbersome and time-consuming, but also rely on specialized reagents and techniques, and are relatively less cost-effective.<sup>5–8</sup> In addition, serum uric acid analysis relies on specialized medical equipment

and involves the invasive procedure of venous blood collection.<sup>9</sup> In contrast, urinalysis, as a non-invasive test, has the potential for rapid diagnosis and prediction of diseases in the clinical setting, and is therefore expected to become a new means of uric acid testing.<sup>10,11</sup>

In the field of uric acid sensors, commercially available products commonly utilize electrochemical detection methods, attributed to their high sensitivity.<sup>12,13</sup> However, conventional electrochemical methods are susceptible to interference from other molecules in complex biological fluids, which can affect detection accuracy.<sup>14</sup> To solve this problem, the introduction of nanomaterials has significantly improved the immunity of the sensors, but they are still subject to complex modification procedures.<sup>15,16</sup> In contrast, uricase (UOx) exhibits significant advantages in enzymatic sensing schemes due to its high specificity for uric acid and resistance to interference. However, UOx lacks metal cofactors, leading to inefficient electron transfer and consequently influencing electrochemical signal generation.<sup>17,18</sup> To overcome this challenge, researchers typically employ a two-enzyme system strategy, whereby concomitant enzymes capable of decomposing hydrogen peroxide (H<sub>2</sub>O<sub>2</sub>), such as horseradish peroxidase (HRP), a common byproduct of the oxidoreductase reaction, are introduced to effectively eliminate their interference with uric acid detection.<sup>19,20</sup> This approach is also applicable to UOx-based uric acid sensors. In recent years, numerous studies have reported the results of uric acid detection using the UOx-HRP dual enzyme system on different detection systems. However,

*a* State Key Laboratory of Cardiology and Medical Innovation Center, Shanghai East Hospital, The Institute for Biomedical Engineering & Nano Science, School of Medicine, Tongji University, Shanghai, 200092, P.R. China.

*b* School of Biomedical Engineering, Shanghai Jiao Tong University, Shanghai, 200030, P.R. China.

\*Corresponding author: yilongwang@tongji.edu.cn

<sup>1</sup> These authors contributed equally to this work.

† Electronic Supplementary Information (ESI) is available: other TEM, DLS, EDS, TMB, and optimization and mass spectrometry data. See DOI: 10.1039/x0xx00000x

1  
2  
3  
4  
5  
6  
7  
8  
9  
10  
11  
12  
13  
14  
15  
16  
17  
18  
19  
20  
21  
22  
23  
24  
25  
26  
27  
28  
29  
30  
31  
32  
33  
34  
35  
36  
37  
38  
39  
40  
41  
42  
43  
44  
45  
46  
47  
48  
49  
50  
51  
52  
53  
54  
55  
56  
57  
58  
59  
60

## ARTICLE

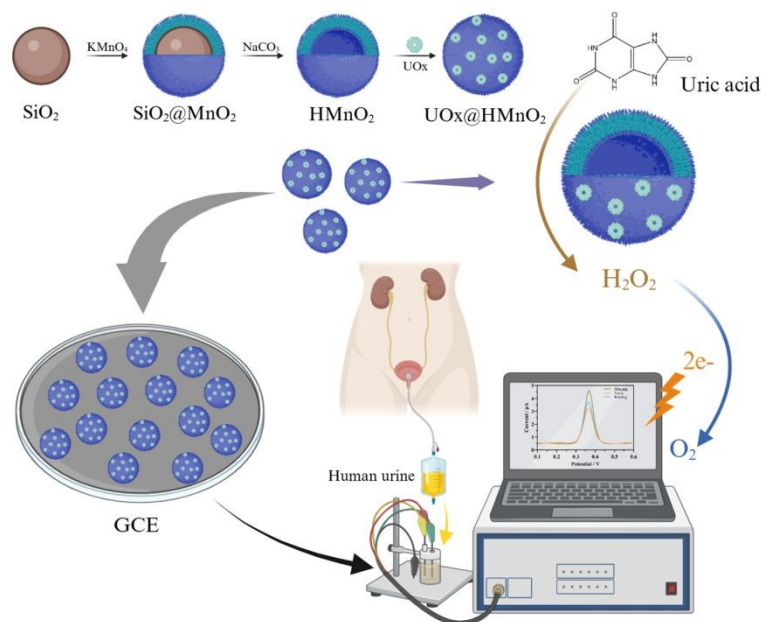


**Fig. 1** Schematic representation of the preparation and catalytic enhancement of uric acid redox signaling by the bio-enzyme-nanozyme biosensor  $\text{UOx}@\text{HMnO}_2/\text{GCE}$ .

there are still some problems with this method, such as the high cost of HRP and the lack of stability of free UOx and HRP.<sup>21,22</sup> Nanozymes, such as iron oxide nanoparticles ( $\text{Fe}_3\text{O}_4$  NPs), have attracted much attention in recent years as a class of innovative nanomaterials with intrinsic enzymatic activity.<sup>23-25</sup> Among them,  $\text{MnO}_2$  nanozymes are particularly prominent for their excellent  $\text{H}_2\text{O}_2$  decomposition mimetic enzyme activity, which can effectively catalyze the decomposition of  $\text{H}_2\text{O}_2$  into water and oxygen.<sup>26,27</sup> Compared with natural enzymes,  $\text{MnO}_2$  nanozymes not only have lower cost, but also have the advantages of tunable catalytic activity, stable structure, unique surface chemistry as well as easy recycling and large-scale preparation.<sup>28,29</sup> In addition,  $\text{MnO}_2$  nanozymes are able to maintain higher catalytic activity for a longer period of time and are less prone to agglomeration or deactivation compared to gold nanoparticles and  $\text{Fe}_3\text{O}_4$  NPs.<sup>30-33</sup> Specifically structured  $\text{MnO}_2$  nanozymes, such as  $\text{MnO}_2$  nanoflowers and hollow  $\text{MnO}_2$ , also exhibit highly efficient drug-carrying capacity, making them ideal carriers for biological enzymes.<sup>34</sup> In particular, hollow  $\text{MnO}_2$  nanozymes are able to protect biomolecules from harsh environments and reduce the leakage of loadings due to their stable porous and hollow structures, which allow the transfer of substances such as electrons.<sup>35,36</sup> This property not only improves the stability of the biological enzyme, but also promotes efficient diffusion, transfer and

reaction of the substrate or intermediate, which in turn improves the mass transfer efficiency and assay accuracy.<sup>37</sup> In this study, we innovatively utilized  $\text{MnO}_2$ , which has peroxidase-mimicking activity, as a protective shell to encapsulate natural uric acid oxidase (UOx), realizing the organic combination of nanozymes and biological enzymes (Fig. 1). The results showed that UOx was able to selectively catalyze the substrate uric acid (UA) and produce  $\text{H}_2\text{O}_2$ , while effectively reducing the interference of common biomolecules such as ascorbic acid, dopamine, L-norepinephrine, glucose, and lactate etc. In addition, the  $\text{MnO}_2$  nanozymes were able to compensate for the absence of metal cofactors or concomitant enzymes in UOx to efficiently reduce  $\text{H}_2\text{O}_2$ . Due to the cascade effect,  $\text{UOx}@\text{MnO}_2$  exhibited an ultra-high activity, which was 4.39 times higher than that of the equivalent  $\text{MnO}_2$ . Ultimately, the prepared  $\text{UOx}@\text{HMnO}_2/\text{Glassy Carbon Electrode}$  (GCE)-based uric acid sensor exhibited high sensitivity and good stability with a detection limit as low as  $0.74 \mu\text{M}$ . Therefore, this study may provide a simple and versatile method for fabricating efficient hybrid biocatalysts in the fields of biosensors and biocatalysis.

## Experimental

### Materials

All chemicals and reagents were of the highest commercially available grade and were used at the price at the time of receipt. Tetraethyl orthosilicate (TEOS), ethanol, hydrogen peroxide (H<sub>2</sub>O<sub>2</sub>, 30% aqueous solution), potassium permanganate (KMnO<sub>4</sub>) and sodium carbonate (Na<sub>2</sub>CO<sub>3</sub>) were purchased from Shanghai (China) Reagent Co. Uric acid, dopamine, L-ascorbic acid, potassium ferrocyanide (K<sub>4</sub>Fe(CN)<sub>6</sub>), potassium ferricyanide (K<sub>3</sub>Fe(CN)<sub>6</sub>), potassium chloride (KCl), (3-Aminopropyl) triethoxysilane (APTES) and uricase were purchased from Sigma-Aldrich (USA). Uricase purchased from Aladdin (China).

### Apparatus

All electrochemical measurements were performed on a CHI660E (Shanghai Chenhua Instrument Co., Ltd.).

### Synthesis of SiO<sub>2</sub> nanoparticles

SiO<sub>2</sub> nanoparticles were prepared by Stöber's method: 50 mL of ethanol was added to a 100 mL flask, followed by 2 mL of deionized water, 2 mL of ammonia under magnetic stirring, after mixing the solution, 3 mL of TEOS was added, and the reaction was continued with stirring for 6 h. Finally, SiO<sub>2</sub> nanoparticles were obtained by centrifugation with ethanol (12,000 rpm) for three times. Amination of SiO<sub>2</sub> nanoparticles: 500 mg of SiO<sub>2</sub> nanoparticles were dispersed in a mixture of 45 mL of ionized water and 100 mL of ethanol, stirred for 5 min and then 0.5 mL of APTES was added to the reaction. After stirring for 1 h at room temperature, the reaction was heated at 80°C for 2 h, and after the reaction solution was cooled down to room temperature, the SiO<sub>2</sub>-NH<sub>2</sub> nanoparticles were obtained by centrifugal washing with ethanol for 3 times.

### Synthesis of hollow manganese dioxide nanoparticles (HMnO<sub>2</sub>)

SiO<sub>2</sub>@MnO<sub>2</sub> nanoparticles synthesis: 200 mg of SiO<sub>2</sub>-NH<sub>2</sub> nanoparticles were dispersed in 100 mL of deionized water and sonicated in a water bath for 10 min. Subsequently, drop by drop KMnO<sub>4</sub> (50 mL, 20 mg mL<sup>-1</sup>) solution was added to the reaction solution under ultrasonic stirring, and the reaction was continued with stirring for 12 h. SiO<sub>2</sub>@MnO<sub>2</sub> nanoparticles were obtained by washing with deionized water for 3-6 times. The prepared SiO<sub>2</sub>@MnO<sub>2</sub> was dissolved in aqueous Na<sub>2</sub>CO<sub>3</sub> solution (2 M) and allowed to stand at 60°C for 6 h. Hollow manganese dioxide nanoparticles HMnO<sub>2</sub> were obtained after centrifugal washing with deionized water for 3 times.

### Synthesis of UOx@HMnO<sub>2</sub>

For UOx loading, 2U of UOx loaded on HMnO<sub>2</sub> (1 mg) for UOx payloading rate and catalytic efficiency. 1 mg of HMnO<sub>2</sub> was dispersed in 1 mL of deionized water, followed by the addition of 100 µg of UOx, and then the reaction was turned over overnight. The nanoparticles were subsequently centrifuged and washed three times to obtain UOx@HMnO<sub>2</sub>. The supernatant from each wash was collected to determine the concentration of UOx eluted, and the loading rate was determined by differential subtraction.

### Characterization

Dynamic light scattering (DLS) measurements were carried out using a Zetasizer Nano-ZS (Malvern, UK) with a standard 633 nm laser at

298.0 K. A JEM-2010 transmission electron microscope (TEM) was used to characterize the morphology of the nanoparticles. High-angle annular dark field scanning TEM (HAADF-STEM) images and elemental maps were obtained by Titan Themis 60-300 G2. UV-Vis spectra of different samples were recorded by UV-Vis spectrophotometer Lambda 35 (Perkin-Elmer).

### Preparation of Electrodes

1 mg of prepared UOx@HMnO<sub>2</sub> was uniformly dispersed in 1 mL of deionized water. 5 µL of the above solution was dropped on the surface of the working electrode and dried under infrared light.

### Electrochemical Measurements

All electrochemical measurements were performed on CHI660E with an electrolyte of 0.1 M KCl, 5 mM [Fe(CN)<sub>6</sub>]<sup>3-/4-</sup> for Cyclic Voltammetry (CV), Electrochemical Impedance Spectroscopy (EIS) and Differential Pulse Voltammetry (DPV). A glassy carbon electrode was used as the working electrode, and a silver/silver chloride reference electrode was set as the reference electrode. The counter electrode was a platinum wire counter electrode.

## Results and discussion

### Synthesis and characterization of UOx@HMnO<sub>2</sub>

The synthesis pathway of hollow manganese dioxide nanoparticles (HMnO<sub>2</sub>) is detailed in Fig. 1.<sup>35</sup> Firstly, SiO<sub>2</sub>@HMnO<sub>2</sub> composites with shell-core structure were constructed by a well-designed synthesis strategy using SiO<sub>2</sub> spheres with a diameter of 100 nm as a template (Fig. S1). Subsequently, the chemical etching effect of sodium bicarbonate was utilized to precisely remove the SiO<sub>2</sub> cores, resulting in hollow manganese dioxide nanoparticles (HMnO<sub>2</sub>) with good monodispersity. Transmission electron microscopy (TEM) observations clearly revealed the unique hollow structure (Fig. 2a). The hollow nanoparticles have a hydrodynamic diameter of about 140 nm and a zeta potential value of -30 mV, indicating excellent dispersion stability (Fig. S2a). Then, the UOx@HMnO<sub>2</sub> composites were successfully prepared by mixing uric acid oxidase (UOx) with HMnO<sub>2</sub>. The TEM images visualized the typical morphology features of UOx@HMnO<sub>2</sub>, and the results showed that the original homogeneous hollow structure of HMnO<sub>2</sub> was preserved without any significant change in the UOx loading process (Fig. 2b). In addition, the hydrodynamic diameter of the composites was increased to 190 nm and the zeta potential was tuned to -20 mV (Fig. S2b), reflecting that the successful introduction of UOx had a slight effect on the material properties. To further investigate the morphological features and elemental composition of UOx@HMnO<sub>2</sub>, high-angle annular dark-field scanning transmission electron microscopy (HAADF-STEM) combined with elemental mapping technique was used for in-depth analysis. The results show that in the prepared UOx@HMnO<sub>2</sub>, the elements Mn and O, as well as the N element derived from UOx, presents clear elemental signals (Fig. 2c). These elemental signals are also further confirmed by energy dispersive spectroscopy (EDS) recordings (Fig. S3), demonstrating the successful preparation of hollow manganese dioxide nanoparticles (UOx@HMnO<sub>2</sub>) loaded with UOx and their structural features as expected.

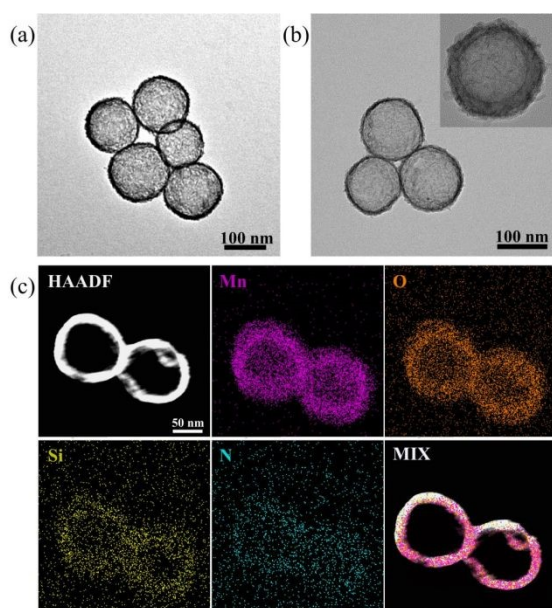


**Fig. 2** Fabrication and characterization of UOx@HMnO<sub>2</sub>. (a) Representative TEM images of HMnO<sub>2</sub> and (b) UOx@HMnO<sub>2</sub>, with insets indicating higher multiples of UOx@HMnO<sub>2</sub>. (c) STEM image of UOx@HMnO<sub>2</sub> showing the elemental distribution of Mn, O, Si and N in it.

To further clarify the structure and chemical composition of UOx@HMnO<sub>2</sub>, we characterized UOx@HMnO<sub>2</sub> using X-ray diffraction (XRD) and X-ray photoelectron spectroscopy (XPS). From the XRD patterns, we clearly observed that HMnO<sub>2</sub> exhibits sharp and distinct characteristic diffraction peaks (Fig 3a). This indicates that we successfully prepared HMnO<sub>2</sub> with the characteristics of the crystal structure of MnO<sub>2</sub>. The XRD peaks of HMnO<sub>2</sub> did not change significantly before and after the loading of UOx. This phenomenon indicates that the loading process of UOx did not significantly affect the crystal structure of HMnO<sub>2</sub>, *i.e.*, the lattice structure of HMnO<sub>2</sub> remained relatively stable. Through XPS analysis, we obtained high-resolution spectra of each element in UOx@HMnO<sub>2</sub>, and determined the presence of Mn, O, C, and N and their chemical states (Fig 3b). Among them, the Mn 2p spectra showed typical MnO<sub>2</sub> characteristic peaks (Fig 3c), and the N 1s spectra helped to determine the presence of UOx in the composite (Fig 3d).

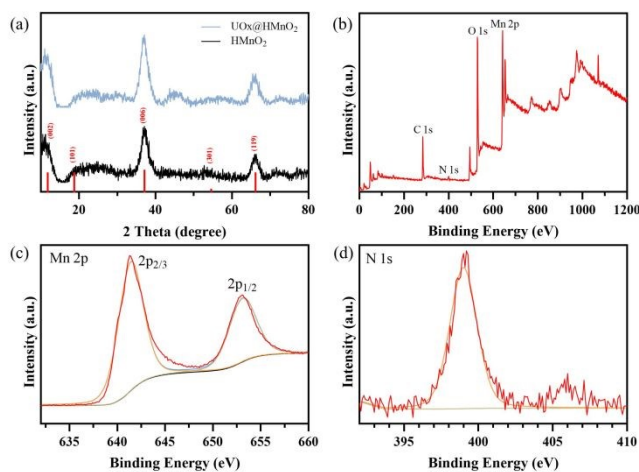


**Fig. 3** Structure and chemical composition of UOx@HMnO<sub>2</sub>. (a) XRD plots of HMnO<sub>2</sub> and UOx@HMnO<sub>2</sub>. (b) XPS spectra of UOx@HMnO<sub>2</sub>. (c) Mn2p spectrum of UOx@HMnO<sub>2</sub>. (d) N1s spectrum of UOx@HMnO<sub>2</sub>.

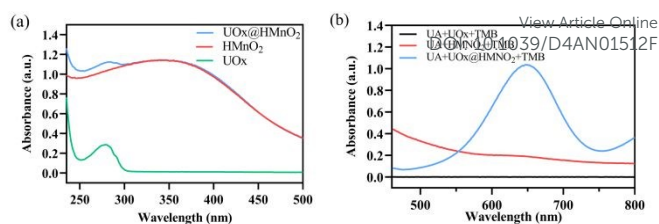


**Fig. 4** Catalytic properties of UOx@HMnO<sub>2</sub>. (a) UV-Vis absorption spectra of free UOx, HMnO<sub>2</sub> and UOx@HMnO<sub>2</sub>. (b) UV-Vis absorption spectra of the catalytic oxidation of TMB (oxTMB) catalyzed by 50 μg mL<sup>-1</sup> UOx@HMnO<sub>2</sub> and 10 μL H<sub>2</sub>O<sub>2</sub> in reaction buffer (pH 6.5).

### Catalytic properties of UOx@HMnO<sub>2</sub>

To check the payload of nanocarriers on UOx, the UV-vis absorption spectra of pure UOx, HMnO<sub>2</sub> and UOx@HMnO<sub>2</sub> are shown in Fig. 4a. The UV absorption peak exhibited by UOx@HMnO<sub>2</sub> at 280 nm was identical to that of pure UOx, indicating that the UOx loading was successful. In addition, the loading of HMnO<sub>2</sub> on UOx was calculated by determining the elution amount of UOx using the BCA method, and its payload was 1.24 w/w% (Table 1). HMnO<sub>2</sub> loaded with UOx exhibits efficient H<sub>2</sub>O<sub>2</sub> conversion. In order to investigate its catalytic activity, we investigated the ability of UOx@HMnO<sub>2</sub> to generate ·OH in 10 μM UA solution, specifically by observing the oxidation of TMB to oxTMB (Fig. S4). This process was confirmed by the UV-Vis absorption spectra, especially the change of the absorption peak at 652 nm (Fig. 4b). These experimental results fully demonstrated that the material possesses not only excellent oxidase activity but also excellent peroxidase activity.

Although we have demonstrated that UOx@HMnO<sub>2</sub> is capable of converting UA to ·OH, the difference between its catalytic activity and that of free UOx has not been clarified. It is worth noting that UOx converts UA to H<sub>2</sub>O<sub>2</sub>, while UOx@HMnO<sub>2</sub> directly generates ·OH through a cascade reaction. To compare the difference in catalytic activity between the two, we used an equivalent amount of HMnO<sub>2</sub> to convert the H<sub>2</sub>O<sub>2</sub> produced by free UOx to ·OH. We also compared the difference in the UV absorption of UOx+HMnO<sub>2</sub> with that of UOx@HMnO<sub>2</sub> through a TMB experiment. We found that compared to free uric acid oxidase, UOx@HMnO<sub>2</sub> catalyzed the generation of H<sub>2</sub>O<sub>2</sub> from uric acid was only slightly weakened, but still maintained a high catalytic activity (Fig. S5).

**Table 1** Loading amounts and loading efficiencies of UOx by 100 μg HMnO<sub>2</sub> at 2U UOx input.

Add amount (μg)	Found amount (μg)	Loading amount (μg)
2.45	1.21±0.079	1.24±0.084

Open Access Article. Published on 23 February 2015. Downloaded on 2/23/2015 10:23:11 AM. This article is licensed under a Creative Commons Attribution-NonCommercial 3.0 Unported Licence.



### Electrochemical study of prepared UOx@HMnO<sub>2</sub>/GCE electrodes

CV and EIS methods were used to analyze the electrochemical behavior of the different modified biosensors. Fig. 5a shows the CV curves with distinct redox separation peaks obtained at GCE, HMnO<sub>2</sub>/GCE and UOx@HMnO<sub>2</sub>/GCE in the presence of 5 mM [Fe(CN)<sub>6</sub>]<sup>3-/4-</sup> containing 0.1 M KCl with a fixed scan rate of 50 mV s<sup>-1</sup>. The modification of the GCE surface with HMnO<sub>2</sub> and UOx@HMnO<sub>2</sub> resulted in a slight change in the peak cathodic and anodic currents compared to GCE, which could be attributed to the "blocking" of the electrode due to the multiple modifications. However, this repulsive effect was very limited and did not significantly change the difficulty of charge transfer between the electrode surface and the [Fe(CN)<sub>6</sub>]<sup>3-/4-</sup> solution. Fig. 5b shows the Nyquist plots of the GCE electrode, HMnO<sub>2</sub>/GCE, and UOx@HMnO<sub>2</sub>/GCE. The calculated R<sub>ct</sub> values for the three electrodes are 241.30, 706.60, and 712.53 Ω. This is attributed to the conformational change of the electrode surface due to the increase in the thickness of the modified layer. This indicates that HMnO<sub>2</sub> and UOx@HMnO<sub>2</sub> have been successfully immobilized on the GCE electrode. Therefore, the fabrication of UOx@HMnO<sub>2</sub> electrode was completely successful.

In 0.1 M KCl solution (pH=7.0) containing 5 mM concentration of [Fe(CN)<sub>6</sub>]<sup>3-/4-</sup> solution at different scan rates ranging from 50 to 300 mV s<sup>-1</sup>, a cyclic voltammetry (CV) to deeply investigate the electron transfer properties of this redox pair at the UOx@HMnO<sub>2</sub>/GCE interface. The results showed that the peak currents (I<sub>p</sub>) of the redox reaction, including the anodic peak current (I<sub>pa</sub>) and cathodic peak current (I<sub>pc</sub>),<sup>40</sup> showed a corresponding increasing trend with the gradual increase of the scanning rate of the UOx@HMnO<sub>2</sub>/GCE electrode (Fig. 5c). In particular, the ratio of anodic (I<sub>pa</sub>) to cathodic (I<sub>pc</sub>) peak currents was close to 1:1 at a scanning rate of 100 mV s<sup>-1</sup>, a result that demonstrated the remarkable quasi-reversibility feature of the redox reaction within the UOx@HMnO<sub>2</sub>/GCE electrode system. In addition, with the accelerated scanning rate, the potential corresponding to the I<sub>pa</sub> was shifted to the positive direction, while the potential corresponding to the I<sub>pc</sub> was shifted to the negative direction, which led to the increase of the peak separation potential (ΔE), and further verified the quasi-reversibility of the redox process occurring on the surface of the electrodes from experimental point of view (Fig. 5d).

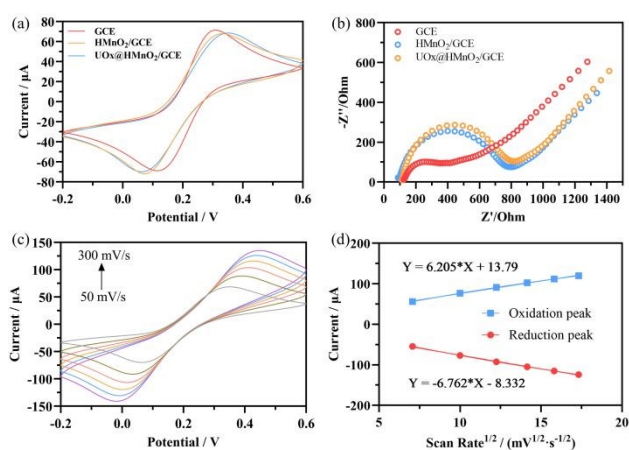


**Fig. 5** Electrochemical study of prepared UOx@HMnO<sub>2</sub>/GCE electrodes. (a) CV plots of GCE, HMnO<sub>2</sub> and UOx@HMnO<sub>2</sub> electrodes in conditions containing 5 mM [Fe(CN)<sub>6</sub>]<sup>3-/4-</sup> and 0.1 M KCl. (b) EIS plots of GCE, HMnO<sub>2</sub> and UOx@HMnO<sub>2</sub> electrodes in 5 mM [Fe(CN)<sub>6</sub>]<sup>3-/4-</sup> indicator solution containing 0.1 M KCl. (c) CV analysis of UOx@HMnO<sub>2</sub>/GCE electrodes at different scan rates and (d) corresponding calibration plots.

### UA detection using UOx@HMnO<sub>2</sub>/GCE electrodes

View Article Online

DOI: 10.1039/D4AN01512F

In order to investigate the effect of the amount of electrically modified materials on electrochemical measurements, working electrodes were assembled on GCE electrodes with 3 μL, 5 μL and 7 μL of UOx@HMnO<sub>2</sub>, respectively. The results show that when the input is 5 μL, a more satisfactory current value and specific surface area are obtained under different CV conditions to achieve the best catalytic effect. (Fig. 6a) The possible reason for this result is due to the balance between the impedance and the catalytic performance of the material immobilized on the surface of the working electrode. That is, the more material piled up on the electrode surface, the more loss of the active surface of the material. And not enough material piled up on the electrode surface, the catalytic capacity failed to reach the peak. Therefore, the input of 5 μL was chosen for modifying the GCE.

Additionally, the pH of the electrolyte solution has a great influence on the performance of enzyme biosensors.<sup>41</sup> Fig. 6b shows the influence of different pH values at a fixed concentration of UA (50 μM). As the pH value decreased from 8.5 to 5.7, the peak current increased significantly, which was attributed to the fact that MnO<sub>2</sub> had the better catalytic performance under acidic conditions,<sup>42</sup> although uricase remained stable in the wide pH range of 5.5 to 10.0 (kept at 25 °C for 16 h). Therefore, pH 5.7 was chosen as the optimal pH condition.<sup>43,44</sup>

DPV was used to study the responses of UOx@HMnO<sub>2</sub>/GCE and HMnO<sub>2</sub>/GCE electrodes to the increase in the concentration of UA (10 to 1000 μM) in a PBS solution with a pH of 5.7 at a scan rate of 100 mV s<sup>-1</sup>. The results are shown in Fig. 7a, b. The DPV curves show the increasing current response of the UOx@HMnO<sub>2</sub>/GCE and HMnO<sub>2</sub>/GCE biosensors over the entire concentration range. That is, the current values increased with increased uric acid concentration. The HMnO<sub>2</sub>/GCE electrode also exhibited a linearly increasing oxidation peak at a +0.3 V potential, but did not respond at lower concentrations of UA (Fig. 7c). The UOx@HMnO<sub>2</sub>/GCE electrode (Fig. 7d), on the other hand, displays a clear and well-defined UA oxidation peak at a potential of +0.35 V, which tends to increase consistently with increasing UA analyte concentration, and demonstrates excellent UA detection performance. It has a stronger current response signal. The peak current (μA) versus uric acid concentration (μM) is also plotted in Fig. S6. From this plot, it can be seen that the UOx@HMnO<sub>2</sub>/GCE electrode has two regions (linear and nonlinear), while the HMnO<sub>2</sub>/GCE electrode has a continuous linear region (Fig. 7e). Typically, the nonlinear region represents the saturation of the current response of the UOx@HMnO<sub>2</sub>/GCE sensor to these.

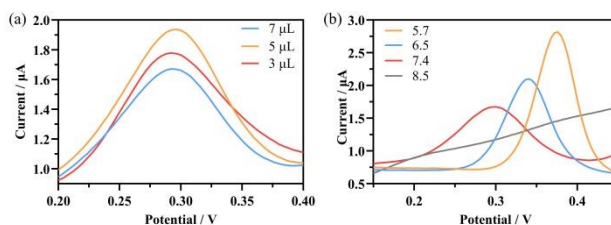


**Fig. 6** CV plots of UOx@HMnO<sub>2</sub>/GCE in PBS solution, Sweep speed: 100 mV s<sup>-1</sup> (a) different volumes, (b) different pH.

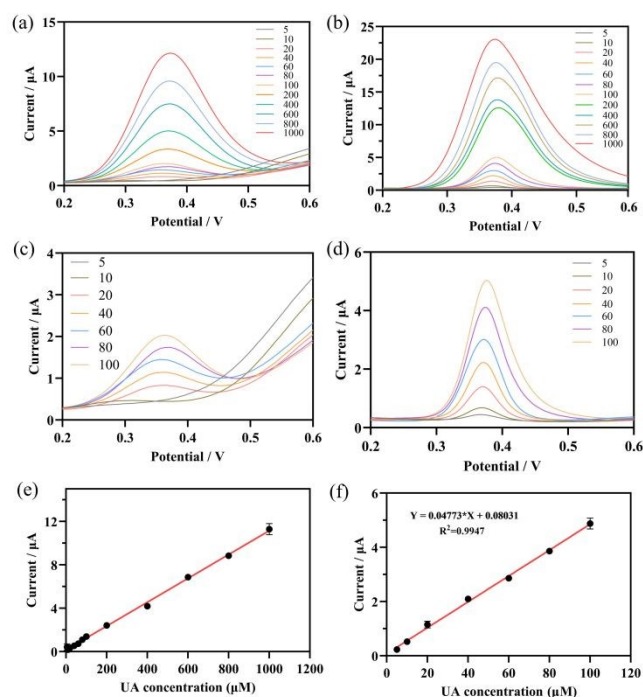


**Fig. 7** Current response of DPV to (a) HMnO<sub>2</sub> and (b) UOx@HMnO<sub>2</sub> modified electrodes at different concentrations of UA (10-1000 μM). Current response of DPV to (c) HMnO<sub>2</sub> and (d) UOx@HMnO<sub>2</sub> modified electrodes at low UA concentrations (10-100 μM) and (e, f) linear relationship between UA concentration and current.

uric acid concentrations (high uric acid concentrations). In addition, the linear region of the sensor response was taken and plotted on a calibration graph (peak current (μA) versus uric acid concentration (μM)) as shown in the Fig. 7f. The sensor responded linearly ( $R^2 = 0.9947$ ) to uric acid concentrations up to 100 μM. In addition, the limit of detection (LOD) was 0.75 μM according to the  $3\sigma$  rule.<sup>45,46</sup> The good sensing performance was attributed to the strong oxidase and peroxidase catalytic ability of UOx@HMnO<sub>2</sub>/GCE.

#### Stability and anti-interference testing

Meanwhile, to determine the stability and reproducibility of the UOx@HMnO<sub>2</sub>/GCE electrode, independent experiments were repeated on 100 μM UA. The results are shown in Fig. 8a. The RSD was 3.56%, respectively, which indicates that the electrode has good reproducibility. In the long-term storage stability test, we placed the prepared sensor at 4°C at different time points and recorded the response current signal of the sensor. As shown in Fig. S7 results, the response signal of the sensor showed only 6.43% fluctuation during the 30-day storage period, which remained within the acceptable error range, indicating that our sensor has good long-term storage stability. The specificity or anti-interference properties of PUM were also evaluated. First, 1 mL of buffer solution was added to UOx@HMnO<sub>2</sub>/GCE, and after the electrode current was stabilized, 10 μL of 1 mM of various interfering substances were added gradually. The stabilized currents before and after the addition of the interfering substances were compared. The results in Fig. 8b show that a significant signal response can only be induced by UA, while the other control samples could not induce any significant signal response. This excellent specificity can be attributed to the UOx-assisted catalytic electrochemical sensing mechanism employed, which also ensures better immunity to interference in clinical urine samples that can be directly detected without any pre-treatment.

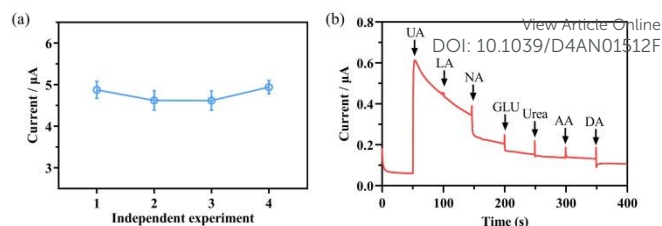


**Fig. 8** Stability and anti-interference testing. (a) Current response values of 4 replicate independent experiments for 100 μM UA. (b) IT curve after addition of 6 interfering substances (10 μM).

#### Detection of UA from real urine samples with UOx@HMnO<sub>2</sub>/GCE biosensors

Urine is an essential biofluid and contains many important metabolites that can convey physiological information relevant to the organism. Therefore, we evaluated the ability of the developed sensors for practical applications in urine detection. As shown in Fig. 9a, we collected real urine samples from a healthy volunteer at three time points (morning, noon, and evening). And the detection of UA was carried out using the UOx@HMnO<sub>2</sub>/GCE biosensor in PBS solution at pH 5.7. The results show that DPV responds to UA in urine with clearly visible signal peaks at three different time points (Fig. 9b). The calculated UA levels detected in urine at the three time points were  $3.998 \pm 0.127$ ,  $2.802 \pm 0.136$  and  $3.227 \pm 0.086$  μM, respectively. This trend is consistent with the result in a study by Xing et al. in which the participants in serial uric acid tests had the lowest levels of uric acid at noon (11:30 a.m.), in the case of either after consumption of high-purine and high-protein foods or with a normal daily diet.<sup>17</sup> The above results indicate that our prepared sensor can be used in human urine under different physiological conditions.

To further confirm the accuracy of the developed UOx@HMnO<sub>2</sub>/GCE biosensor for the detection of uric acid in urine, we compared the results with those obtained using mass spectrometry. This is due to the fact that mass spectrometry is the gold standard technology in the field of detection due to its high sensitivity and accuracy. Specifically, we determined the concentration of uric acid in real urine samples using high performance liquid chromatography-tandem mass spectrometry (UHPLC-MS/MS) (Fig. 9c). Using toluenesulfonylurea as an internal standard, chromatographic peaks from uric acid were detected (Fig. S8), and their true concentrations were calculated from the standard curves to be  $2.839 \pm 0.126$ ,  $4.169 \pm 0.160$ , and  $3.185 \pm 0.075$  mM, respectively (Fig. 10a). Compared with our prepared UOx@HMnO<sub>2</sub>/GCE biosensor, no significant difference was found using paired t-test (Fig. 10b). These results indicate that the method possesses comparable detection capability to mass spectrometry and can be used to accurately detect uric acid content in actual urine samples.

## Analyst

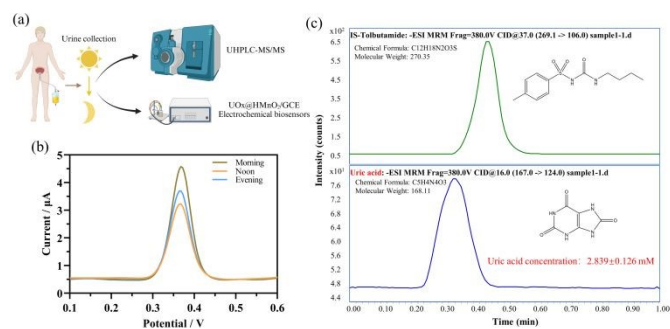


**Fig. 9** Detection of real samples with UOx@HMnO<sub>2</sub>/GCE biosensors. (a) Schematic diagram of human urine sample collection and testing. (b) Current response of DPV to UOx@HMnO<sub>2</sub>/GCE electrode in urine collected at different time points. (c) Uric acid concentration in human urine samples was determined using high performance liquid chromatography-tandem mass spectrometry (UHPLC-MS/MS).

Spiking recovery experiments are essential for assessing the accuracy and reliability of the assay in the analysis of real samples and can be used as a complementary validation of the UOx@HMnO<sub>2</sub>-GCE and UHPLC-MS/MS comparison means. We selected three actual samples. A known concentration of uric acid standard (10 μM, 20 μM, and 40 μM) was added to each sample, which was then assayed according to our established assay method. The results showed that the recoveries ranged from 96.00% -103.27%, which indicated that our assay had good accuracy and reliability in the analysis of real samples and could effectively detect the real content of uric acid in the samples (Table S1).

To make a comparison between our sensor and previously reported sensors for UA detection, as shown in the table 2, it is clear that our sensor exhibited better performance than the conventional sensors in terms of limit of detection, and is able to achieve accurate detection of much smaller amounts of uric acid. However, the linear range is relatively narrow, which maybe due to the fact that UOx@HMnO<sub>2</sub>-GCE has two linear regions. The concentration and trend of UA in the actual samples after being diluted were proved consistent with those measured by UHPLC-MS/MS, which can meet the need of detecting a wider range of concentration. Moreover, in terms of selectivity, UOx@HMnO<sub>2</sub>-GCE can tolerate interfering substances and maintain a stable detection performance over a longer period of time.

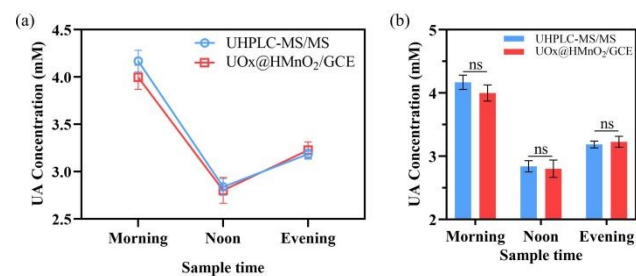


**Fig. 10** (a) Curve and (b) T-test analysis of uric acid concentration in real samples at three time points detected by UOx@HMnO<sub>2</sub>/GCE electrode and UHPLC-MS/MS.

**Table 2** Comparison of analytical performance of UOx@HMnO<sub>2</sub>-GCE with other uric acid testing techniques

View Article Online  
DOI: 10.1039/D4AN01512F

Methods	Detection range	LOD	R <sup>2</sup>	Ref
Electrochemical	50-1000 μM	18.7 μM	0.998	18
Electrochemical	0-4 mM	8.87 μM	0.9933	17
Colorimetric	0.5-6 mM	0.25 mM	0.9922	25
Electrochemical	0-1.6 mM	11.4 μM	0.9898	15
Electrochemical	2-500 μM	0.411 μM	0.998	14
Electrochemical	100-1000 μM	1 μM	0.9956	47
Electrochemical	0.2-50 μM	0.067 μM	0.994	48
Electrochemical	0-1000 μM	—	0.9978	16
Colorimetric	1-50 μg/mL	—	0.9995	49
LC-MS/MS	0.06-30 μM	0.15 μM	0.9993	7
This study	5-100 μM	0.74 μM	0.9947	/

## Conclusions

Focusing on the important field of uric acid detection, this study explores the many problems faced by existing detection methods and uric acid sensors and achieves remarkable results. The core innovation of the study is the successful construction of the UOx@HMnO<sub>2</sub> composite system. By wrapping natural uric acid oxidase (UOx) with MnO<sub>2</sub> nanozyme, which has peroxidase mimetic activity, as a protective shell, the organic combination of nanozyme and biological enzyme was realized. In this system, UOx can specifically catalyze the production of H<sub>2</sub>O<sub>2</sub> from uric acid substrate and effectively reduce the interference of common biomolecules such as ascorbic acid, dopamine, L-norepinephrine, glucose, and lactic acid, while MnO<sub>2</sub> nanozymes make up for the lack of metal cofactors in UOx, and efficiently catalyze the decomposition of H<sub>2</sub>O<sub>2</sub>. The cascade effect produced by the synergy of the two resulted in the sensitivity of the UOx@HMnO<sub>2</sub> uric acid sensor as high as 0.74 μM with good stability. In the future, the results of this research are expected to be further expanded and deepened in the structure-property relationship of the MnO<sub>2</sub> composite system, the expansion of the material application, and the translation of the clinical application.

## Author contributions

Chenlong He: conceptualization, investigation, validation, and writing of original draft. Huawei Liu: investigation, validation, and writing review & editing. Ming Yin: conceptualization, methodology, investigation, and writing original draft. Jing Chen: conceptualization, methodology and writing original draft. Wensi Huang: investigation, validation. Han Zhou: conceptualization, and writing of original draft. Shengming Wu: writing of original draft and writing review & editing. Yilong Wang: writing review & editing, supervision, project administration and funding acquisition.



## Conflicts of interest

There are no conflicts of interest to declare.

## Data availability

The data supporting this article have been included as part of the ESI.

## Acknowledgements

This work was supported by the National Natural Science Foundation of China (Grant Nos.32271439, 32071395).

## Notes and references

- S. Wen, H. Arakawa and I. Tamai, PHARMACOLOGY & THERAPEUTICS, 2024, **256**, 108615.
- L. Zheng, H. Ma, Y. Ma, Q. Meng, J. Yang, B. Wang, Y. Yang, W. Gong and G. Gao, INTERNATIONAL JOURNAL OF ELECTROCHEMICAL SCIENCE, 2019, **14**, 9573–9583.
- L. Du, Y. Zong, H. Li, Q. Wang, L. Xie, B. Yang, Y. Pang, C. Zhang, Z. Zhong and J. Gao, SIGNAL TRANSDUCTION AND TARGETED THERAPY, 2024, **9**, 212.
- Y. Zhao, T. Ye, H. Liu, Y. Kou, M. Li, Y. Shao, Z. Zhu and Q. Zhuang, FRONTIERS IN BIOSCIENCE-LANDMARK, 2006, **11**, 2976–2982.
- X. Luo, N. Cai and Z. Cheng, Analytical Sciences, 2013, **29**, 709–713.
- W. Huang, J. Yu and X. Diao, Journal of Pharmaceutical and Biomedical Analysis, 2023, **224**, 115188.
- X.-Y. Liu, Y. Luo, C.-Y. Zhou, A. Peng and J.-Y. Liu, Bioanalysis, 2017, **9**, 1751–1760.
- W. Huang, W. Li, X. Yu, M. Xue, Y. Yuan, C. Chen, Y. Wu, J. Yu and X. Diao, Journal of Chromatography B, 2024, **1234**, 123991.
- Y. Zhang, H. Yu, S. Chai, X. Chai, L. Wang, W.-C. Geng, J.-J. Li, Y.-X. Yue, D.-S. Guo and Y. Wang, ADVANCED SCIENCE, 2022, **9**, 2104463.
- S. Yeasmin, G. Ammanath, A. Onder, E. Yan, U. H. Yildiz, A. Palaniappan and B. Liedberg, TrAC Trends in Analytical Chemistry, 2022, **157**, 116786.
- N. Balhara, M. Devi, A. Balda, M. Phour and A. Giri, URINE, 2023, **5**, 40–52.
- L. Chelmea, M. Badea, I. Scarneciu, M. A. Moga, L. Dima, P. Restani, C. Murdaca, D. Ciurescu and L. E. Gaman, Chemosensors, 2023, **11**, 341.
- L. Hao, X. Li, H. Liang, W. Lei, W. Yang and B. Zhang, Microchimica Acta, 2024, **38**, 191. DOI:10.1007/s00604-023-06113-2.
- Y. Liu, Y. Zhang, C. Wang, X. Zeng, J. Lei, J. Hou, D. Huo and C. Hou, ACS Appl. Nano Mater., 2024, **7**, 6273–6283.
- R. Stephanie, D. Y. Lee, C. Y. Park and T. J. Park, ANALYST, 2023, **148**, 1442–1450.
- S. Masrat, V. Nagal, M. Khan, I. Moid, S. Alam, K. S. Bhat, A. Khosla and R. Ahmad, Biosensors, 2022, **12**, 1140.
- X. Xing, B. Yao, Q. Wu, R. Zhang, L. Yao, J. Xu, G. Gao and W. Chen, Biosensors and Bioelectronics, 2022, **198**, 113804.
- S. H. Han, Y.-J. Ha, E. H. Kang, K. Shin, Y. J. Lee and G.-J. Lee, Scientific Reports, DOI:10.1038/s41598-022-16176-5.
- Y. Zhang, S. Tsitkov and H. Hess, Nature Catalysis, 2018, **1**, 276–281.
- A. Chellachamy Anbalagan and S. N. Sawant, Microchimica Acta, 2021, **11**, 188. DOI:10.1007/s00604-021-05059-7.
- M. Dai, T. Huang, L. Chao, Q. Xie, Y. Tan, C. Chen and W. Meng, Talanta, 2016, **149**, 117–123.
- Y. Jiao, Y. Xing, K. Li, Z. Li and G. Zhao, Luminescence, 2021, **36**, 1110–1116.
- W. Yang, X. Yang, L. Zhu, H. Chu, X. Li and W. Xu, Coordination Chemistry Reviews, 2021, **448**, 214170.
- M. Yin, L. Zhang, Y. Chen, S. Qi, X. Wei, X. Tian, J. Qiu and D. Xu, MATERIALS CHEMISTRY AND PHYSICS, 2022, **282**, 125992.
- T. Leelasattarathkul, T. Trakoolwilaiwan and K. Khachornsakkul, Analyst, 2024, **149**, 5518–5526.
- S. Sisakhtnezhad, M. Rahimi and S. Mohammadi, Biomedicine & Pharmacotherapy, 2023, **163**, 114833.
- B. Song, Z. Wang, H. Yan, X. Zhang, Q. Liu, J. Luo and J. Yuan, The Analyst, 2024, **149**, 3547–3554.
- A. M. Ashrafi, Z. Bytesnikova, J. Barek, L. Richtera and V. Adam, Biosensors and Bioelectronics, 2021, **192**, 113494.
- M. Li, T. Zhang and Y. Zhang, The Analyst, 2023, **148**, 2180–2188.
- H. Yuan, J. Chen, Y. Guo, H. Wang and P. Hu, J. Phys. Chem. C, 2018, **122**, 25365–25373.
- S. Xiong, R. Tang, D. Gong, Y. Deng, C. Zhang, J. Zheng, M. Zhong, L. Su, L. Yang and C. Liao, Applied Materials Today, 2020, **21**, 100798.
- Y. Wang, F. Wang, B. Chen, H. Xu and D. Shi, Chem. Commun., 2011, **47**, 10350–10352.
- H.-Y. Xia, B.-Y. Li, Y. Zhao, Y.-H. Han, S.-B. Wang, A.-Z. Chen and R. K. Kankala, Coordination Chemistry Reviews, 2022, **464**, 214540.
- Q. Yang, Y.-Y. Mao, Q. Liu and W.-W. He, Rare Metals, 2023, **42**, 2928–2948.
- H. Ji, C. Zhang, F. Xu, Q. Mao, R. Xia, M. Chen, W. Wang, S. Lv, W. Li and X. Shi, Advanced Science, 2022, **9**, 2201696.
- C. Lin, H. Zhang, X. Zhang, Y. Liu and Y. Zhang, ACS Appl. Mater. Interfaces, 2023, **15**, 14388–14398.
- G. Yang, L. Xu, Y. Chao, J. Xu, X. Sun, Y. Wu, R. Peng and Z. Liu, Nature Communications, 2017, **1**, 8. DOI:10.1038/s41467-017-01050-0.
- S. A. A. Noma, Process Biochemistry, 2023, **131**, 52–58.
- Y.-C. Chiu, T.-S. Hsu, C.-Y. Huang and C.-H. Hsu, International Journal of Biological Macromolecules, 2021, **188**, 914–923.
- Q. Yan, N. Zhi, L. Yang, G. Xu, Q. Feng, Q. Zhang and S. Sun, SCIENTIFIC REPORTS, 2020, **10**, 10607.
- W. Liu, D. Zhang, F. Zhang, Z. Hao, Y. Li, M. Shao, R. Zhang, X. Li and L. Zhang, Analyst, 2023, **148**, 1579–1586.
- M. Wekesa and Y. H. Ni, TAPPI JOURNAL, 2003, **2**, 23–26.
- D. Iswantini, N. Nurhidayat, Trivadila and O. Widiyatmoko, Pakistan journal of biological sciences: PJBS, 2014, **17**, 277–81.
- D. Iswantini, N. Nurhidayat, Trivadila and E. Mardiah, Jurnal Ilmu Pertanian Indonesia, 2009, **14**, 163–169.
- J. Chen, L. Hao, J. Hu, K. Zhu, Y. Li, S. Xiong, X. Huang, Y. Xiong and B. Z. Tang, Angewandte Chemie, 2022, **7**, 134, DOI:10.1002/ange.202112031.
- J. Chen, L. Hao, Y. Wu, T. Lin, X. Li, Y. Leng, X. Huang and Y. Xiong, Chem. Commun., 2019, **55**, 10312–10315.
- M. Yang, H. Wang, P. Liu and J. Cheng, Biosensors and Bioelectronics, 2021, **179**, 113082.
- G. Ren, F. Dong, Z. Zhao, K. Li and Y. Lin, ACS Appl. Mater. Interfaces, 2021, **13**, 52987–52997.
- Y. Bai, X. Fan, G. Chen and Z. Zhao, Anal. Methods, 2024, **16**, 5896–5901.

# Data availability statements

View Article Online  
DOI: 10.1039/D4AN01512F

The data supporting this article have been included as part of the Electronic Supporting Information (ESI).

1  
2  
3  
4  
5  
6  
7  
8  
9  
10  
11  
12  
13  
14  
15  
16  
17  
18  
19  
20  
21  
22  
23  
24  
25  
26  
27  
28  
29  
30  
31  
32  
33  
34  
35  
36  
37  
38  
39  
40  
41  
42  
43  
44  
45  
46  
47  
48  
49  
50  
51  
52  
53  
54  
55  
56  
57  
58  
59  
60

Open Access Article Published on 24 February 2025. Downloaded on 2/23/2025 10:23:11 AM.  
This article is licensed under a Creative Commons Attribution-NonCommercial 3.0 Unported Licence.



Analyst Accepted Manuscript